Advances in Technology Innovation, vol. 11, no. 4, 2026, pp. 479-499

Systematic Design and Performance Evaluation of LCL-Filtered Grid-Forming Inverters under Different Operating Conditions

Melad Nasser Abdulahad, Yasir Mohammed Younis Ameen*, Basil Mohammed Saied

Department of Electrical Engineering, College of Engineering, University of Mosul, Mosul, Iraq

Received 10 May 2026; revised 20 July 2026; accepted 22 July 2026

DOI: https://doi.org/10.46604/aiti.2026.16442

Abstract

This study aims to develop a systematic design for inductor-capacitor-inductor (LCL)-filtered grid-forming inverters (GFMIs) and evaluates their performance under various operating scenarios. The proposed methodology presents the mathematical modeling of GFMI in the dq reference frame, designs the LCL filter parameters within a stable resonance-frequency region, and employs a bandwidth-coordination scheme to design cascaded current and voltage controllers. Small-signal stability analysis based on eigenvalues is used to assess stability under varying grid strength and parameter variations. Results from MATLAB/Simulink show that the proposed design provides stable operation and acceptable dynamic performance in both grid-connected and stand-alone modes. Furthermore, the inverter output voltage and current achieve low total harmonic distortion (THD) of 4.3% and 1.2%, respectively, at rated load. Although current THD increases under light-load grid-connected mode, the total demand distortion (TDD) remains below 5% for all tested conditions, thereby satisfying the requirements of IEEE Standard 519.

Keywords: grid-forming inverters, LCL filter, cascaded controllers, resonance frequency, stability

1. Introduction

Grid-connected inverters (GCIs) are employed to integrate renewable energy sources (RESs), such as photovoltaic and wind energy systems, into the utility grid. Among the main control technologies used for GCIs are grid-forming inverters (GFMIs) and grid-following inverters (GFLIs). GFMIs have emerged as a promising alternative to GFLIs owing to their ability to establish voltage without relying on the grid voltage, operate effectively in both grid-connected mode (GCM) and stand-alone mode (SAM), and provide virtual inertia [1].

To comply with grid connection requirements, the inverter output voltage should be maintained as close as possible to a pure sinusoidal waveform. Therefore, an inductor-capacitor-inductor (LCL) filter is usually employed to attenuate the high-frequency harmonics generated by the switching process. Compared with an L-type filter, the LCL filter is preferred because it requires smaller passive components and provides a higher harmonic attenuation rate [2].

However, GFMIs may be exposed to abnormal operating conditions. Owing to the intermittent nature of RESs, these inverters are often required to operate under light-load conditions. Moreover, grid outages in GCM and load outages in SAM can force GFMIs to operate under no-load conditions [3]. Under these conditions, the LCL filter characteristics may change, resulting in resonance. This behavior introduces disturbances and harmonic distortion into the output voltage, thereby affecting system stability [4]. In severe cases, overvoltage may exceed the rated levels and cause serious failure of the inverter components [5].

* Corresponding author. E-mail address: yasir_752000@uomosul.edu.iq

Several studies have investigated LCL filter design and resonance mitigation techniques. In [2], different passive damping schemes based on the placement of a damping resistor were evaluated, and the series connection of the damping resistor with the filter capacitor branch was identified as an effective solution. In [6], a comparative study was conducted to determine suitable LCL filter component values using a conventional design methodology while maintaining filter stability and efficiency for various voltage source converter (VSC) applications.

Active damping methods have also been proposed to suppress the resonance of the LCL filter. In [7], the authors proposed an active disturbance rejection control method based on pole-zero cancellation and a reduced-order extended state observer to mitigate the resonance effect of the LCL filter. The results showed that the proposed method remained effective under grid-impedance variations without the need for controller retuning, while providing higher stability margins. In [8], inverter-side current feedback (ISCF) was adopted because of its inherent damping capability. The effect of delay was also considered in the design process, since it limits the stability region of the resonance frequency when ISCF is employed. In [9], the authors proposed an active damping strategy based on the principle of equivalent transformation to address the shift in the natural resonance peak of the LCL filter. The results showed good performance under both strong and ultra-weak grid conditions.

A related study in [10] proposed a control structure that naturally suppresses LCL-filter resonance without adding passive damping components or separate active damping loops. Sliding-mode control (SMC) was employed, where the sliding surface was generated from the capacitor-voltage error, while the capacitor-voltage reference was obtained through a proportional-resonant (PR) controller. Additionally, the study focused on improving grid-current tracking and chattering reduction. However, the authors noted that although the boundary-layer SMC method reduces chattering and stabilizes the switching frequency, selecting the boundary-layer thickness requires a trade-off between tracking accuracy and robustness.

Nevertheless, the combined SMC–PR control structure requires slightly more implementation effort than a conventional PI-based structure. As reported by [11], some PR discretization methods involve trigonometric calculations that increase the computational burden and require additional processing resources. Furthermore, the performance of a PR controller can be affected by deviations in grid frequency, which may introduce attenuation and phase error [12]. Therefore, the present study employs passive damping and conventional PI controllers to facilitate practical implementation and to provide a systematic design procedure.

In the control structure of GFMIs, interactions among controllers should also be considered. The authors in [13] studied the impact of feedforward terms in the outer voltage loop on GFMI stability. They showed that these terms can affect the small-signal stability if the inner current loop is not fast enough. To improve the stability, retuning the PI-gains of the voltage controller and attenuating the feedforward gains were suggested. However, such solutions may require continuous monitoring of system parameters to achieve adaptive adjustment, which increases the complexity of the control system. The study in [14] recommended bandwidth coordination; however, it did not provide supporting analysis or validate the proposed method through simulation or experimental validation.

To compare the present study with existing GCI studies, a comparative analysis is presented in Table 1, covering system configuration, operating technique, filter and controller design, damping approach, bandwidth coordination, stability assessment, grid strength, abnormal operating conditions, validation method, and power-quality performance.

Based on the above literature and the comparison presented in Table 1, most previous studies have focused on addressing individual aspects of GCI design, such as selecting suitable LCL filter parameters, developing damping techniques to mitigate resonance under grid-impedance variations, or designing advanced control methods. However, among the studies compared, limited attention has been given to a systematic design of LCL-filtered GFMIs that integrates the design of both the LCL filter and cascaded controllers. Furthermore, an explicit coordinated design scheme for LCL filter parameters with resonance-frequency constraints has not been provided, while bandwidth coordination between the inner and outer control loops has not

been sufficiently investigated to reduce loops interaction. In addition, performance evaluation under abnormal operating conditions, particularly light-load and no-load conditions, has received limited attention. Stability analysis of the complete system, including plant and controller dynamics, has also received limited attention in the studies considered.

Table 1 Comparative assessment of GCI studies based on design, control, stability, and performance

Design and performance criteria	[4]	[6]	[10]	[15]	[16]	[17]	Proposed work
System configuration (1-ph/ 3-ph)	— / ✓	— / ✓	✓ / —	— / ✓	— / ✓	— / ✓	— / ✓
Operating technique (GFL/ GFM)	— / ✓	✓ / —	NR / NR	— / —	NR / NR	✓ / —	— / ✓
Step-by-step design (filter/controller)	— / ✓	— / ✓	— / ✓	✓ / —	✓ / —	✓ / —	✓ / ✓
Provision of an LCL filter design scheme based on resonance constraints	—	—	—	△	△	△	✓
Damping approach (passive/ active/ inherent)	— / ✓ / —	— / ✓ / —	— / — / ✓	✓ / — / —	✓ / — / —	✓ / — / —	✓ / — / —
Controller types (inner/ outer)	PI / PI	Observer-based OSMC	SMC / PR	— / —	PI / PI	PI / PI	PI / PI
Explicit bandwidth coordination between cascaded loops	△	—	—	—	—	—	✓
Complete-system stability analysis (plant + controllers)	TD	Bode plot + TD	TD	TD	TD	Impedance Bode + TD	Eigenvalue + TD
Grid strength (very weak/ weak/ strong)	NR/ NR/ NR	✓ / ✓ / —	NR/ NR/ NR	NR/ NR/ NR	NR/ NR/ NR	✓ / ✓ / ✓	✓ / ✓ / ✓
Abnormal conditions (no-load or light-load/ unbalance)	— / —	— / ✓	— / NA	— / —	— / —	— / —	✓ / —
Validation (simulation/ experiment)	✓ / —	✓ / ✓	✓ / —	✓ / ✓	✓ / ✓	✓ / —	✓ / —
Power-quality (THDv/ THDi/ TDDi)	✓/ NR / NR	NR /✓/ NR	NR /✓/ NR	NR/ ✓ / NR	✓ / ✓ / NR	NR /✓/ NR	✓ / ✓ / ✓

Note. ✓ = explicitly considered or clearly addressed; △ = partially considered or addressed in a related context; — = not considered; NA = not applicable; NR = not reported. For multi-entry cells, the order follows the terms listed in parentheses in the corresponding criterion. Abbreviations: OSMC, optimal sliding-mode control; TD, time domain.

To fill these gaps, this study presents a systematic design for LCL-filtered GFMIs. The proposed approach provides a step-by-step LCL-filter design scheme based on resonance-frequency constraints, thereby maintaining the resonance frequency within the stable region and avoiding resonance excitation. In addition, a bandwidth-coordination scheme is adopted for the cascaded current and voltage control loops to reduce loops interaction and improve the dynamic performance. Furthermore, eigenvalue-based small-signal stability analysis of the designed system is conducted under different grid-strength conditions together with a parameter sensitivity analysis. Finally, the designed GFMI is evaluated through time-domain simulations in both GCM and SAM under rated-load, light-load, and no-load conditions.

2. Mathematical Modeling of the GFMI and Design of the LCL Filter

In this section, the mathematical model and design of the grid-forming inverter with an LCL filter are described. First, the modulation index of space vector pulse-width modulation (SVPWM) is formulated in the dq-frame. Next, the dynamic model of the GFMI is presented. Then, the stable resonance-frequency region of the LCL filter is determined. Finally, the LCL filter design procedure is introduced.

2.1 Modulation index of SVPWM in the dq-frame

The relationship between the line-to-neutral voltage V_{LN} and the corresponding dq-frame voltage components is illustrated in Fig. 1 and given by:

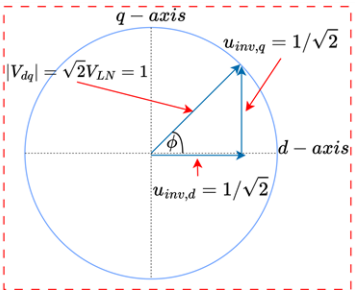


Fig. 1 Phasor diagram illustrating the relationship between the phase voltage (V_{LN}) and voltage components ($u_{inv,d}$, $u_{inv,q}$)

$$V_{LN} = \frac{|V_{dq}|}{\sqrt{2}} = \frac{u_{inv,d} + ju_{inv,q}}{\sqrt{2}} = \frac{\sqrt{u_{inv,d}^2 + u_{inv,q}^2}}{\sqrt{2}} \tag{1}$$

where $|V_{dq}|$, $u_{inv,d}$, and $u_{inv,q}$ denote the peak phase voltage, the inverter terminal voltage in d-axis, and the inverter terminal voltage in q-axis, respectively. When the SVPWM strategy is employed, the modulation index can be obtained using [18]:

$$m = \frac{\sqrt{6}V_{LN}}{V_{dc}} \tag{2}$$

where V_{dc} denotes the DC-bus voltage. The phase angle between $u_{inv,d}$ and $u_{inv,q}$ voltage components is then computed by:

$$\phi = \tan^{-1}\left(\frac{u_{inv,q}}{u_{inv,d}}\right) \tag{3}$$

2.2 Mathematical model of the GFMI with LCL filter

Applying Kirchhoff's voltage law to the LCL filter loops shown in Fig. 2 and neglecting the effect of the damping resistor (R_f), the following equations are obtained:

$$u_{inv,abc} = r_1 i_{1,abc} + L_1 \frac{di_{1,abc}}{dt} + u_{c,abc} \tag{4}$$

$$u_{c,abc} = r_2 i_{2,abc} + L_2 \frac{di_{2,abc}}{dt} + u_{pcc,abc} \tag{5}$$

where u_{inv}, u_c, and u_{pcc} represent the inverter voltage, capacitor voltage, and point-of-common-coupling voltage, respectively, while u_{grid} represents the grid voltage. In addition, i_1 and i_2 represent the inverter-side current and grid-side current, respectively. The subscript '*abc*' denotes the three-phase quantities in the stationary reference frame. Transforming Eqs. (4) and (5) from the stationary frame into the synchronous frame using Park's transformation yields:

$$u_{inv,d} = r_1 i_{1,d} + L_1 \frac{di_{1,d}}{dt} - \omega L_1 i_{1,q} + u_{c,d} \tag{6a}$$

$$u_{inv,q} = r_1 i_{1,q} + L_1 \frac{di_{1,q}}{dt} + \omega L_1 i_{1,d} + u_{c,q} \tag{6b}$$

$$u_{c,d} = r_2 i_{2,d} + L_2 \frac{di_{2,d}}{dt} - \omega L_2 i_{2,q} + u_{pcc,d} \tag{7a}$$

$$u_{c,q} = r_2 i_{2,q} + L_2 \frac{di_{2,q}}{dt} + \omega L_2 i_{2,d} + u_{pcc,q} \tag{7b}$$

where the subscript '*dq*' denotes the direct and quadrature quantities in the rotating reference frame at the grid angular frequency ω.

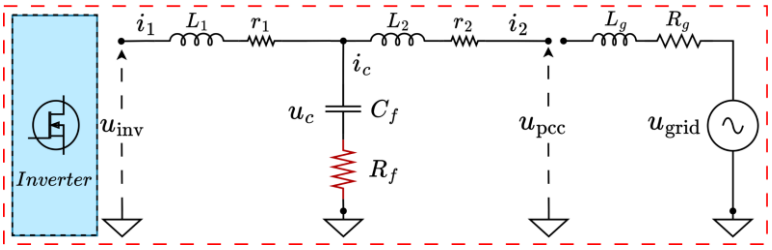


Fig. 2 Single-line diagram of the three-phase GFMI with an LCL filter

The capacitor current (i_c) can be derived by applying Kirchhoff's current law at the capacitor node, as illustrated in Fig. 2, and is expressed as follows:

$$i_{c,abc} = i_{1,abc} - i_{2,abc} = C_f \frac{du_{c,abc}}{dt} \tag{8}$$

Similarly, transforming Eq. (8) into the synchronous frame gives:

$$i_{c,d} = C_f \frac{du_{c,d}}{dt} - \omega C_f u_{c,q} \tag{9a}$$

$$i_{c,q} = C_f \frac{du_{c,q}}{dt} + \omega C_f u_{c,d} \tag{9b}$$

Therefore, Eqs. (6a)-(7b) and Eqs. (9a)-(9b) describe the dynamic interactions among the inverter, LCL filter, and utility grid.

2.3 Definition of the stable resonance-frequency region for the LCL filter

Using Eqs. (4), (5), and (8), the transfer function between the output current and the input voltage of the LCL filter can be derived, as given in:

$$\frac{i_2}{u_{inv}} = \frac{C_f R_f s + 1}{L_1 L_2 C_f s^3 + C_f \left(L_1 \left(r_2 + R_f\right) + L_2 \left(r_1 + R_f\right)\right) s^2 + \left(L_1 + L_2 + C_f \left(r_1 r_2 + r_1 R_f + r_2 R_f\right)\right) s + \left(r_1 + r_2\right)} \tag{10}$$

Then, the resonance frequency of the LCL filter is obtained by setting the denominator of Eq. (10) equal to zero, and considering the worst-case condition by assuming $r_1 = r_2 = R_f = 0$, and it is given by:

$$f_{res} = \frac{1}{2\pi} \sqrt{\frac{1}{L_2 C_f} + \frac{1}{L_1 C_f}} \tag{11}$$

while the resonance frequency under light-load, no-load, or high grid impedance conditions is calculated by using Eq. (11) and considering the grid-side inductance approaches infinity ($L_2 \to \infty$), and it is expressed by:

$$f_{res(L_2 \to \infty)} = \frac{1}{2\pi} \frac{1}{\sqrt{L_1 C_f}} \tag{12}$$

Therefore, the maximum and minimum resonance frequency ($f_{res,max}$ and $f_{res,min}$) are determined from the designed LCL filter parameters and grid impedance using Eqs. (11) and (12), respectively. In order to operate in a stable region, the resonance frequency of the LCL filter should be chosen to be greater than ten times the grid frequency ($10 f_g$) and smaller than half of the switching frequency ($0.5 f_{sw}$), as recommended in [15]. Thus, these design constraints can be expressed as:

$$f_{c,\min} = 10 f_g \ < \ f_{res,\min} \le f_{res} \le f_{res,\max} \ < \ f_{c,\max} = f_{sw} / 2 \tag{13}$$

where the lower constraint ($f_{c,min}$) prevents the resonance frequency from falling in the low-frequency harmonic range, thus avoiding the amplification of low-order harmonics. The constraint also helps ensure a high control bandwidth, thus allowing a fast dynamic response without oscillations. The upper constraint ($f_{c,max}$) prevents the resonance frequency from approaching the switching frequency region, where switching harmonics can be amplified.

2.4 Design of the LCL filter parameters

The design procedure from [16] is adopted and modified to achieve stable operation under abnormal conditions, and it is described as follows. First, the maximum peak-to-peak ripple of the inverter output current is expressed as:

$$\Delta I_{L,\max} = \frac{V_{dc}}{6 f_{sw} L_1} \tag{14}$$

This ripple current is set between 5% to 25% of the inverter's maximum rated current, as expressed in [19]:

$$\Delta I_{L,\max} = (5\% - 25\%) I_{L,\max} \tag{15}$$

The maximum rated current is calculated using the following equation:

$$I_{L,\max} = \frac{\sqrt{2}P}{\sqrt{3}V_{LL}} \tag{16}$$

where P and V_{LL} are the nominal rated power of the inverter and the line-to-line voltage, respectively. Therefore, the inverter-side inductor L_1 can be calculated by:

$$L_1 = \frac{V_{dc}}{6 f_{sw} \Delta I_{L,\max}} \tag{17}$$

It is worth mentioning that the value of L_1 should not be excessively high in order to prevent an increase in inductor size and cause a significant voltage drop. According to [20], the voltage drop across L_1 should not exceed 10% of the nominal voltage at rated current. Therefore, the maximum limit of L_1 is given by:

$$L_1 \le L_{1,\max} = 0.1 L_b = 0.1 \frac{Z_b}{\omega_b} = 0.1 \frac{V_{LL}^2}{\omega_b P} \tag{18}$$

where L_b, Z_b and ω_b denote the base inductance, base impedance, and base angular frequency, respectively. Second, the filter capacitance should be selected to be less than or equal to 5% of the converter base capacitance (C_b), as given below:

$$C_f = 0.05 C_b = 0.05 \frac{1}{\omega_b Z_b} = 0.05 \frac{P}{\omega_b V_{LL}^2} \tag{19}$$

This constraint is imposed to limit the excessive reactive current absorption and prevent power factor degradation. However, selecting a very small capacitance value requires a larger grid-side inductor to achieve the required filtering performance. Furthermore, the minimum filter capacitance should be selected such that the resonance frequency remains above the minimum allowable limit (i.e., $f_{c,min}$). This value is obtained from Eq. (12) by setting the resonance frequency to $f_{c,min}$, as given by:

$$C_f = \frac{1}{L_1 \left(2\pi f_{c,\min}\right)^2} \tag{20}$$

Therefore, the filter capacitance should be selected within the range specified in:

$$\frac{1}{L_1 \left(2\pi f_{c,\min}\right)^2} < C_f < 0.05 \frac{P}{\omega_b V_{LL}^2} \tag{21}$$

Third, the grid-side inductor is designed based on the attenuation factor of the grid-side current ripple, as expressed below [16]:

$$L_2 = \frac{\sqrt{(1/k_a^2)}+1}{C_f \omega_{sw}^2} \tag{22}$$

where k_a is the desired attenuation factor, which is defined as the ratio of the grid-side current to the inverter-side current at the switching frequency. This factor is selected from the range of 10%- 20%. To meet the upper resonance-frequency constraint of Eq. (13), the grid-side inductor must be selected greater than its minimum value. This minimum value is obtained from Eq. (11) by setting the resonance frequency to $f_{c,max}$, as given by:

$$L_2 = \frac{L_1}{L_1 C_f \left(2\pi f_{c,\max}\right)^2 - 1} \tag{23}$$

Thus, the final value of L_2 is chosen as the greater value between Eqs. (22) and (23) as shown in the following equation to satisfy both the ripple-attenuation requirement and the upper-resonance-frequency constraint:

$$L_2 = max\left(\frac{L_1}{L_1 C_f \left(2\pi f_{c,\max}\right)^2 - 1}, \frac{\sqrt{(1/k_a^2)}+1}{C_f \omega_{sw}^2}\right) \tag{24}$$

Finally, in order to suppress the resonance under light-load or no-load conditions, a damping resistor is connected in series with the filter capacitor, as illustrated in Fig. 2. The damping resistance value is selected based on a trade-off between improving the resonance peak suppression and reducing the power loss. Accordingly, an optimal value is determined to be one-third of the capacitive reactance of the filter capacitor at the resonance frequency, which is achieved by choosing the quality factor Q = 3 and can be defined as [17, 21]:

$$R_f = \frac{1}{Q}\frac{1}{2\pi f_{res(L_2 \to \infty)} C_f} = \frac{1}{3}\sqrt{\frac{L_1}{C_f}} \tag{25}$$

The total power dissipated in the damping resistors is calculated at the fundamental frequency component, as it constitutes the most dominant losses, and is expressed by [22]:

$$P_{loss,R_f} = 3 i_c^2 R_f = 3\left(\frac{u_c}{R_f + 1/\omega_b C_f}\right)^2 R_f \tag{26}$$

3. Design of the Cascaded Controllers for the GFMI

This section presents the design procedure for the cascaded control loops for the GFMI. First, the bandwidth-coordination scheme of the cascaded loops is introduced. Then, the modeling and design of the current and voltage controllers are presented.

3.1 Bandwidth coordination of the cascaded control loops

The typical control structure of a GFMI consists of multiple cascaded control loops, including an inner current loop, a middle voltage loop, and an outer power loop. Proper bandwidth coordination is needed to avoid bandwidth overlap and minimize the mutual interactions among these loops. Therefore, the middle loop should have a lower bandwidth than the inner loop, while the outer loop should have the lowest bandwidth. In the frequency domain, this indicates that each outer loop should operate within the unity-gain region of its preceding inner loop. In the time domain, it means that the inner loop should exhibit the fastest dynamic response, followed by the middle loop and then the outer loop.

According to a common rule of thumb, the bandwidth of the inner loop should be selected below approximately one-tenth of the switching frequency, and the bandwidth of each outer loop also should be approximately ten times lower than that of the preceding loop, as illustrated in Fig. 3 [14]. However, this bandwidth ratio (i.e., 10x) between the inner and outer loops

should be regarded as an initial guideline rather than a strict constraint. The final bandwidth ratio should be determined based on the stability margins and dynamic performance requirements, provided that the outer-loop bandwidth is lower than the inner-loop bandwidth to avoid overlap.

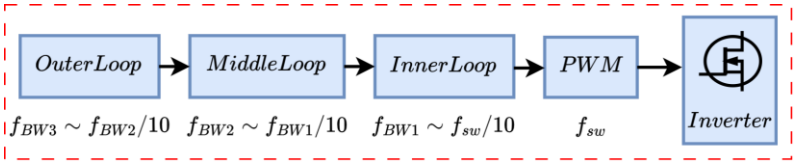


Fig. 3 Cascaded control loops of the GFMI and their bandwidth-coordination scheme

3.2 Current control loop

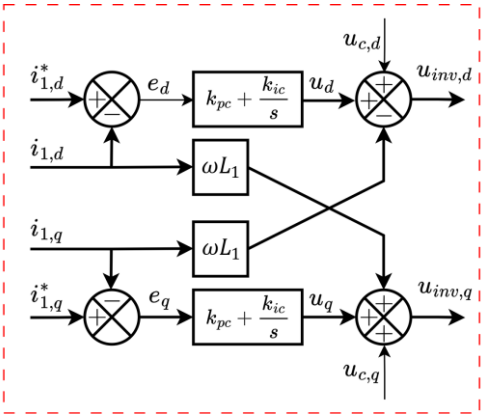


Fig. 4 Implementation structure of the current control loop

The current control loop generates modulation signals that are compared with the carrier signal to produce the inverter switching pulses. In this loop, the measured inverter-side currents are compared with the reference values generated by the voltage control loop. The resulting current errors are processed by the PI controller. The output of the PI controller is then combined with the feedforward voltage and cross-coupling terms to obtain the modulation voltage reference, as illustrated in Fig. 4. Because the d-axis and q-axis have identical control structures and design procedures, only the d-axis current control loop is analyzed for simplicity.

3.3 PI controller design for the current loop

To simplify the PI controller design, both the cross-coupling terms ($\omega L_1 i_{1,d}, \omega L_1 i_{1,q}$) and the feedforward terms ($u_{c,d}, u_{c,q}$) are ignored during the design process to minimize the complexity of the current control model [23]. Accordingly, Eq. (6a) can be simplified to the following equation, where u_d is the voltage corresponding to $u_{inv,d}$ when this simplification is applied to Eq. (6a).

$$u_d = r_1 i_{1,d} + L_1 \frac{di_{1,d}}{dt} \tag{27}$$

The transfer function of the current-control plant can be determined by taking the Laplace transform of Eq. (27) and rearranging the resulting expression to obtain:

$$u_d = r_1 i_{1,d} + L_1 i_{1,d} s \rightarrow \frac{i_{1,d}}{u_d} = \frac{1}{r_1 + L_1 s} \tag{28}$$

The transfer function of the PI controller used in the current loop is defined as follows,

$$u_d = \left(k_{pc} + \frac{k_{ic}}{s}\right) e_d = \left(k_{pc} + \frac{k_{ic}}{s}\right)\left[i_{1,d}^* - i_{1,d}\right] \tag{29}$$

where k_{pc} and k_{ic} represent the proportional and integral gains of the PI controller, respectively, and e_d represents the error obtained from the difference between the reference and measured currents, while the superscript * denotes the reference value. This control loop is affected by the delay introduced by the sampling process and the PWM technique. This delay can be calculated as $T_d = T_{sw} + 0.5T_{sw} = 1.5T_{sw}$, where $T_{sw} = 1/f_{sw}$ denotes the switching period. In the s-domain, the delay is represented by $e^{-T_d s}$. For analytical convenience, it is approximated by the following first-order transfer function:

$$e^{-T_d s} \approx \frac{1}{T_d s + 1} \tag{30}$$

Therefore, the open-loop transfer function of the current control is obtained by combining the PI controller, the current-control plant, and the delay model, as illustrated in Fig. 5, and can be expressed as follows:

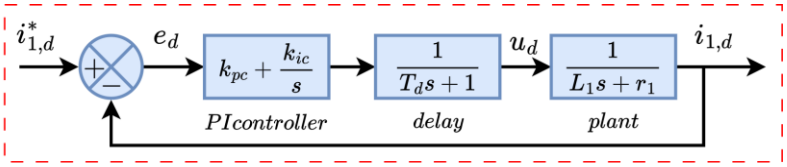


Fig. 5 Block diagram of the current control loop used for analysis and controller design

$$G_{C,O.L.} = \frac{i_{1,d}}{i^*_{1,d}} = \left(k_{pc} + \frac{k_{ic}}{s}\right)\left(\frac{1}{T_d s + 1}\right)\left(\frac{1}{L_1 s + r_1}\right) \tag{31}$$

Rearranging Eq. (31), the zero-pole-gain form of the transfer function can be given by:

$$G_{C,O.L.} = \frac{k_{pc}}{L_1}\left(\frac{s + (k_{ic}/k_{pc})}{s}\right)\left(\frac{1}{T_d s + 1}\right)\left(\frac{1}{s + (r_1/L_1)}\right) \tag{32}$$

Then, to design the PI controller parameters, the pole-zero cancellation method is applied to Eq. (32), which yields:

$$G_{C,O.L.} = \left(\frac{k_{pc}}{L_1}\right)\left(\frac{1}{s}\right)\left(\frac{1}{T_d s + 1}\right) \tag{33}$$

$$\frac{k_{ic}}{k_{pc}} = \frac{r_1}{L_1} \tag{34}$$

The closed-loop transfer function of Eq. (33) is given by:

$$G_{C,C.L.} = \frac{(k_{pc}/T_d L_1)}{s^2 + (1/T_d)s + (k_{pc}/T_d L_1)} \tag{35}$$

By comparing Eq. (35) with the standard second-order closed-loop transfer function and using Eq. (34), the values of k_{pc} and k_{ic} can be obtained as follows, where δ denotes the damping ratio of the second-order system:

$$k_{pc} = \frac{L_1}{4T_d\delta^2} \quad [\Omega] \tag{36}$$

$$k_{ic} = \frac{r_1}{4T_d\delta^2} \quad [\Omega/s] \tag{37}$$

Finally, substituting Eq. (29) into Eq. (27), followed by substitution of the resulting expression into Eq. (6a), yields the implementation equation of the d-axis current control loop. The corresponding equations for both the d-axis and q-axis are given as follows and illustrated in Fig. 4:

$$u_{inv,d} = \left(k_{pc} + \frac{k_{ic}}{s}\right)\left[i^*_{1,d} - i_{1,d}\right] - \omega L_1 i_{1,q} + u_{c,d} \tag{38}$$

$$u_{inv,q} = \left(k_{pc} + \frac{k_{ic}}{s} \right) \left[i_{1,q}^{*} - i_{1,q} \right] + \omega L_1 i_{1,d} + u_{c,q} \tag{39}$$

3.4 Voltage control loop

The voltage control loop is designed to regulate the inverter output voltage. Its operation is similar to that of the current loop. The reference voltage generated by the outer loop, such as the droop controller or the virtual synchronous generator controller, is compared with the measured output voltage. The resulting voltage error is applied to a PI controller. The PI controller output is then combined with the feedforward and cross-coupling terms, as depicted in Fig. 6. The output of this loop is used as the reference current for the inner current control loop.

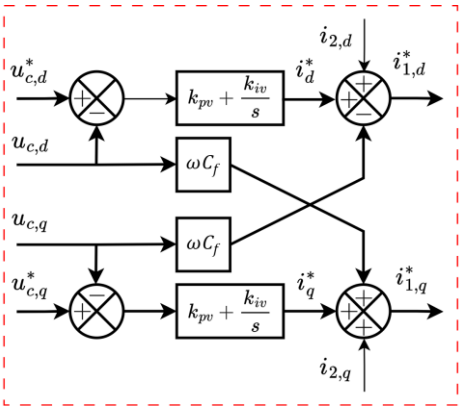


Fig. 6 Implementation structure of the voltage control loop

3.5 PI controller design for the voltage loop

The reference current for the inner current loop is defined as:

$$i_{1,d}^{*} = i_{c,d} + i_{2,d} = C_f \frac{du_{c,d}}{dt} - \omega C_f u_{c,q} + i_{2,d} \tag{40}$$

Following the same simplification used for the current-loop design, the cross-coupling terms ($\omega C_f u_{c,d}, \omega C_f u_{c,q}$) and the feedforward terms ($i_{2,d}, i_{2,q}$) are neglected in Eq. (40), yielding the following formulation:

$$i_d^{*} = C_f \frac{du_{c,d}}{dt} \tag{41}$$

where i_d^{*} denotes the current corresponding to $i_{1,d}^{*}$ after applying the simplification in Eq. (40), and represents the PI controller output. Taking the Laplace transform of Eq. (41), the transfer function of the voltage-control plant is defined by:

$$i_d^{*} = C_f u_{c,d} s \rightarrow \frac{u_{c,d}}{i_d^{*}} = \frac{1}{C_f s} \tag{42}$$

To achieve a more robust voltage-loop design, the effect of the inner current loop is incorporated into the PI-parameter design. This effect is commonly approximated as unity gain. However, a more accurate representation can be obtained by approximating its second-order closed-loop transfer function as a first-order delay system, which can be expressed as [24]:

$$\frac{1}{T_{dc} s + 1} \tag{43}$$

where T_{dc} is the equivalent time constant of the inner current loop, which is equal to twice the time delay (i.e., $T_{dc} = 2T_d$) as reported in [25]. The transfer function of the PI controller for the voltage loop is given by:

$$i_d^* = \left(k_{pv} + \frac{k_{iv}}{s}\right)\left[u_{c,d}^* - u_{c,d}\right] \tag{44}$$

Therefore, the open-loop transfer function of the voltage control loop is obtained by combining the PI controller, the equivalent inner-loop delay model, and the transfer function of the voltage-control plant, as illustrated in Fig. 7. The open-loop transfer function expression is defined as:

$$G_{V,O.L.} = \frac{u_{c,d}}{u_{c,d}^*} = \left(k_{pv} + \frac{k_{iv}}{s}\right)\left(\frac{1}{T_{dc}s+1}\right)\left(\frac{1}{C_f s}\right) \tag{45}$$

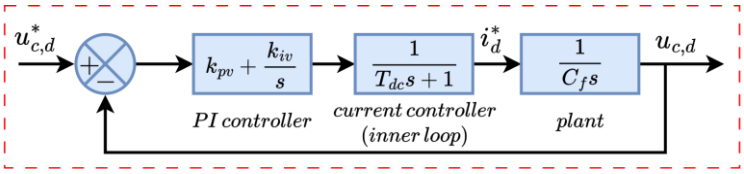


Fig. 7 Block diagram of the voltage control loop used for analysis and controller design

The symmetrical optimum criterion is applied to design the PI parameters of the voltage loop. Accordingly, the proportional and integral gains (k_{pv} and k_{iv}) can be obtained as follows [24-25]:

$$k_{pv} = \frac{C_f}{\sqrt{T_{dc}T_{iv}}} \quad [1/\Omega] \tag{46}$$

$$k_{iv} = \frac{k_{pv}}{T_{iv}} \quad [1/(\Omega s)] \tag{47}$$

$$T_{iv} = a^2 T_{dc} \tag{48}$$

where T_{iv} is the integral time constant of the PI controller, and 'a' is a tunable factor selected to provide an appropriate damping ratio to achieve the desired performance. Therefore, the voltage control loop is implemented by substituting Eq. (44) into Eq. (41) and the resultant expression into Eq. (40). As a result, the implementation equation of the d-axis voltage control loop is obtained. The corresponding d-axis and q-axis equations are given below and illustrated in Fig. 6:

$$i_{1,d}^* = i_{c,d} + i_{2,d} = \left(k_{pv} + \frac{k_{iv}}{s}\right)\left[u_{c,d}^* - u_{c,d}\right] - \omega C_f u_{c,q} + i_{2,d} \tag{49}$$

$$i_{1,q}^* = i_{c,q} + i_{2,q} = \left(k_{pv} + \frac{k_{iv}}{s}\right)\left[u_{c,q}^* - u_{c,q}\right] + \omega C_f u_{c,d} + i_{2,q} \tag{50}$$

4. Results and Discussion

This section evaluates the proposed GFMI design through verification of the LCL-filter design constraints, frequency-response analysis, controller design, small-signal stability assessment, and time-domain simulations. The analysis verifies the resonance-frequency constraints, damping performance, controller bandwidth coordination, stability under grid-strength and parameter variations, and dynamic performance in both GCM and SAM under different loading conditions.

4.1 Design procedure for the LCL filter

The design specifications of the GFMI are listed in Table 2. First, to determine L_1, the desired ripple current is selected as 10% of the rated current, and the switching frequency is set to $f_{sw} = 6\ kHz$. Using Eq. (17), the inverter-side inductor is obtained as $L_1 = 18.284\ mH$. The filter capacitance is then selected as 5% of the base capacitance, and its value is calculated from Eq. (19) as $C_f = 6.613\ \mu F$. The attenuation factor is selected as 10%. Therefore, the grid-side inductance is obtained

from Eq. (22) as $L_2 = 1.17\ mH$. Finally, the damping resistance is calculated using Eq. (25), resulting in $R_f = 17.5\ \Omega$. To verify the resonance-frequency constraint, the corresponding expression is obtained by Eq. (13) as follows:

$$500\ Hz\ <\ 457.7\ Hz \leq f_{res} \leq 1866.0\ Hz\ <\ 3000\ Hz \tag{51}$$

Table 2 Model parameters and design specifications of GFMI

Parameters	Symbol	Value	Unit	Parameters	Symbol	Value	Unit
Line-to-Line grid voltage	V_{LL}	380	V	DC bus voltage	V_{dc}	600	V
Grid frequency	f_{g}	50	Hz	Inverter-side resistor	r_1	0.1	Ω
Grid resistor	R_{g}	0.95	Ω	Grid-side resistor	r_2	0.01	Ω
Grid inductor	L_{g}	19.15	mH	Switching frequency	f_{sw}	20	kHz
Nominal rated power of inverter	P	6	kW	Solver frequency fixed-step (ODE4 RUNGE-KUTTA)	f_{solver}	1	MHz

Eq. (51) shows that the resonance frequency does not fall within the desired limits. Although the upper boundary is achieved, the lower boundary is not met. In addition, the obtained value of L_1 is impractical because it exceeds the maximum limit ($L_{1,\max} = 7.66\ mH$). Therefore, the filter parameters should be redesigned based on the following procedure.

First, to reduce the value of L_1, the switching frequency is increased to $f_{sw} = 20\ kHz$, and the ripple current is adjusted to 20%, resulting in $L_1 = 2.742\ mH$, which is below the maximum limit. Second, the filter capacitance is initially selected to have the same value used in the first design case. Then, the lower resonance-frequency boundary in Eq. (13) is checked. If this condition is not satisfied, the minimum filter capacitance is calculated using Eq. (20) by selecting $f_{res,min}$ to be greater than $f_{c,min}$. Third, the grid-side inductor is calculated using Eq. (22), with the attenuation factor set to 10%, giving $L_2 = 0.1053\ mH$. If the upper resonance-frequency boundary is not satisfied, L_2 is recalculated using Eq. (23). Finally, the damping resistance is calculated as $R_f = 6.788\ \Omega$, which is lower than that obtained in the first design case. After that, the resonance-frequency constraint is verified using the redesigned parameters, as shown below. It confirms that the redesigned parameters satisfy the required limits. The overall design procedure is summarized in the flowchart shown in Fig. 8.

$$500\ Hz\ <\ 1181.7\ Hz \leq f_{res} \leq 6144.9\ Hz\ <\ 10000\ Hz \tag{52}$$

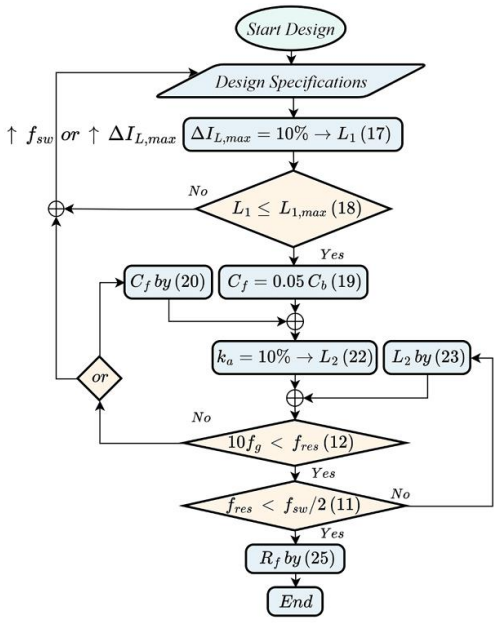


Fig. 8 Proposed flowchart for the design procedure of the LCL filter parameters

The power losses in the damping resistors for both design cases are calculated using Eq. (26), with the per-phase capacitor voltage set to $u_c = 220\ V$. The obtained losses are $P_{loss,R_f} = 10.211\ W$ and $P_{loss,R_f} = 4.136\ W$, respectively, and the corresponding percentages of power dissipated relative to the inverter's rated power are 0.17% and 0.06%. These percentages

are small and acceptable relative to the design criterion limit of [26] (less than 1%), and they indicate that the passive damping approach provides adequate resonance suppression with a limited efficiency penalty.

Using the parameters of the second design case in Eq. (10), the frequency response of the LCL filter under normal operating conditions (on-load) is obtained with and without the damping resistor, as shown in Fig. 9. In addition, the no-load condition is investigated by assuming that the grid-side resistance approaches infinity (i.e., $r_2 = 10\ M\Omega$), and the corresponding frequency responses for both cases with and without the damping resistor are also obtained, as presented in Fig. 9. It can be observed that the resonance frequency falls within the stability boundaries and matches well with the analytical values.

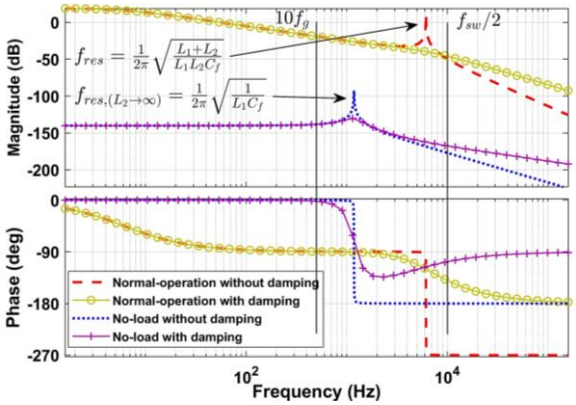
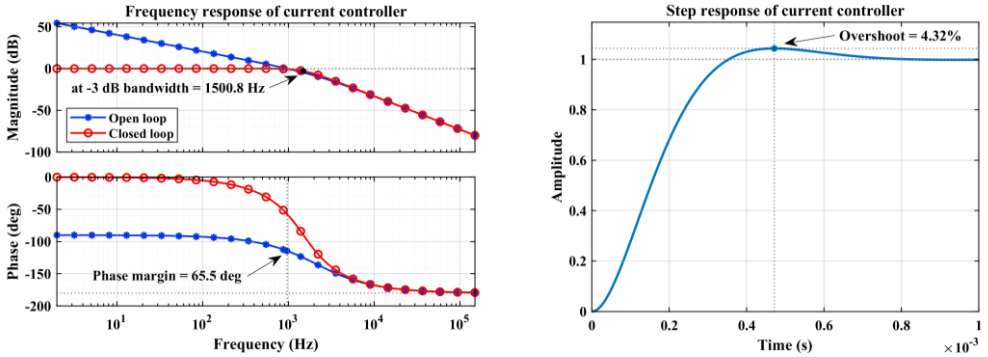


Fig. 9 Frequency response of the LCL filter showing the upper and lower resonance frequencies at $f_{res} = 6143.3\ Hz$ and $f_{res} = 1182.5\ Hz$, respectively

4.2 Design procedure for the current and voltage controllers

First, the current controller is designed by selecting the damping ratio as $\delta = 1/\sqrt{2}$ to achieve optimum response, while setting $L_1 = 2.742\ mH$ and $r_1 = 0.1\ \Omega$. Using Eqs. (36) and (37), the values of k_{pc} and k_{ic} are obtained as 18.28 Ω and 666.66 Ω/*s*, respectively. Next, the voltage-controller parameters are calculated from Eqs. (46) and (47). By selecting a = 3 and setting the filter capacitance to $C_f = 6.613\ \mu F$, the values of k_{pv} and k_{iv} are obtained as 0.01469 1/Ω and 10.88 1/(Ωs), respectively.

The frequency response of the current controller is plotted using Eq. (32), as illustrated in Fig. 10(a). The figure shows that the closed-loop bandwidth is 1500.8 *Hz*, which is lower than the theoretical bandwidth limit (20000/10 = 2000 *Hz*). This indicates that the controller design satisfies the loop-bandwidth coordination requirement illustrated in Fig. 3. In addition, the controller achieves a phase margin of 65.5°, a settling time of 0.63 *ms*, and an overshoot of 4.32%, as shown in Fig. 10(b).

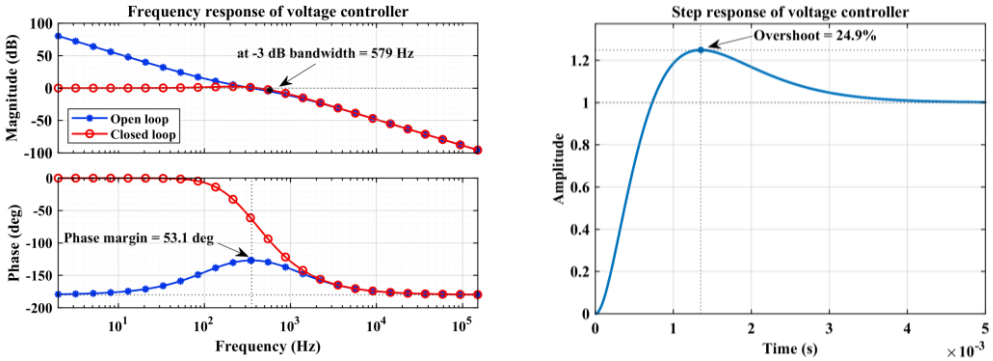


(a) In frequency domain (b) In time domain

Fig. 10 Response of the designed current controller

Fig. 11(a) shows the frequency response of the voltage controller obtained from Eq. (45). The controller has a bandwidth of 579 *Hz*, which is higher than the theoretical bandwidth of the second loop (20000/100 = 200 *Hz*). Although this value does not strictly follow the rule of thumb illustrated in Fig. 3, it remains approximately 2.5 times lower than that of the inner loop,

while the cutoff frequency of this controller remains within the unity-gain region of the inner current loop's magnitude-frequency curve. This indicates limited interaction between the two loops. This deviation from the rule is mainly attributed to the selected value of a = 3, which is tuned to achieve the desired dynamic response of the overall control system. Moreover, this controller has a phase margin of 53.1°, a settling time of 3.55 *ms*, and an overshoot of 24.9%, as shown in Fig. 11(b).



(a) In frequency domain (b) In time domain

Fig. 11 Response of the designed voltage controller

In addition, both controllers have an acceptable phase margin higher than the commonly recommended minimum value of 45°. This confirms that the controller's design has an acceptable stability margin and can provide robust dynamic performance against parameter variations, as stated in [27].

4.3 Eigenvalue-based small-signal stability and parameter sensitivity analysis

To further assess the robustness of the designed system, small-signal stability is evaluated under grid-strength and filter-parameter variations. Eigenvalue analysis is adopted because it provides an efficient method for assessing the stability of systems that have multiple inputs and multiple outputs (MIMO).

In GCM, variations in the utility grid impedance alter the grid-side impedance of the LCL filter. Therefore, the equivalent grid-side impedance is defined as ($Z_e = Z_2 + Z_g$). The utility grid is represented by a Thevenin equivalent consisting of an ideal voltage source in series with the grid impedance, as shown in Fig. 2. For a fixed grid (X_g/R_g) ratio, by substituting $u_{pcc} = V_{LL}$ and assuming unity power factor ($S_{rated} = P$), the corresponding R_g and L_g values can be calculated from a specified short-circuit ratio (SCR) using the following expressions:

$$|Z_g| = \frac{u_{pcc}^2}{SCR \times S_{rated}},\quad R_g = \frac{|Z_g|}{\sqrt{1+(X_g/R_g)^2}},\quad L_g = \frac{(X_g/R_g)R_g}{\omega_b} \tag{53}$$

Using the nominal grid impedance in Table 2 ($R_g = 0.95\ \Omega$ and $L_g = 19.15\ mH$) gives $X_g/R_g = 6.3$ and SCR = 4. This operating point was selected to represent a weak-grid condition with predominantly inductive behavior and to reproduce the conditions investigated in [3]. Such conditions are relevant to low-voltage distribution networks with long feeders and rural networks. However, this condition is not typical of an urban low-voltage grid, which generally has shorter feeders, lower equivalent impedance, and higher SCR, and is therefore considered a strong grid [28]. Consequently, to assess the performance and applicability of the designed GFMI under these grid conditions, an eigenvalue-based stability analysis was conducted at different grid strengths using a 12-state model. The corresponding state-space equation is defined as follows:

$$\Delta\dot{x} = A\Delta x \tag{54}$$

where Δ represents the small-signal perturbation and $A \in \mathbb{R}^{12\times12}$ is the state matrix. The state vector (Δx) includes the six electrical states, the current- and voltage-controller integral states, and the two inverter-voltage delay states, as illustrated by:

$$\Delta x = [i_{1,d}\ i_{1,q}\ u_{c,d}\ u_{c,q}\ i_{2,d}\ i_{2,q}\ \xi_{i,d}\ \xi_{i,q}\ \xi_{v,d}\ \xi_{v,q}\ u_{inv,d}\ u_{inv,q}]^T \tag{55}$$

where the first six electrical state variables are derived from Eqs. (6a)-(7b) and Eqs. (9a)-(9b). Meanwhile, the variables $\xi_{i,d}, \xi_{i,q}, \xi_{v,d}$ and $\xi_{v,q}$ represent the integral states of the d- and q-axis current and voltage-control errors, respectively. The derivative form of $\xi_{i,d}$ is expressed by:

$$\dot{\xi}_{i,d} = (i_{1,d}^{*} - i_{1,d}) \tag{56}$$

The inverter-voltage delay state is obtained by renaming the inverter voltage command represented by Eq. (38) as $u_{cmd,d}$ and the delayed inverter voltage as $u_{inv,d}$. Therefore, the inverter-voltage delay derivative state is given by:

$$\dot{u}_{inv,d} = \frac{1}{T_d}(u_{cmd,d} - u_{inv,d}) \tag{57}$$

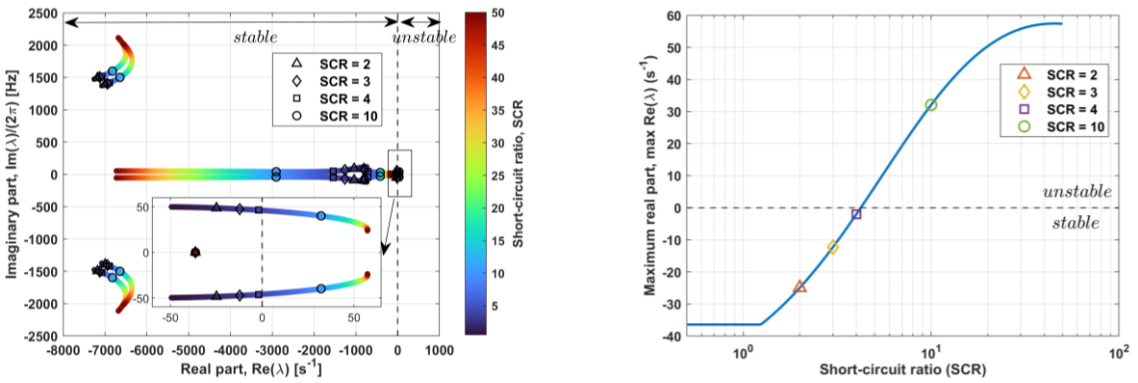
For stability assessment, the eigenvalue-based criterion is defined as $\max_i\{Re[\lambda_i(SCR)]\} < 0,\ i \in 1,\ldots,12$, which indicates that for the system to be stable, the maximum real part of the eigenvalues should be less than zero.

Fig. 12(a) shows the eigenvalue trajectories as the SCR varies over a wide range from 0.5 to 50 for the same X_g/R_g ratio. Most of the high-frequency eigenvalues remain within the left-half plane, whereas the low-frequency conjugate pair poles near the imaginary axis exhibit the largest displacement. As the SCR increases, this pair moves toward the right-half plane and even crosses the stability boundary. Therefore, the loss of stability is associated with the dominant low-frequency poles rather than the high-frequency poles.

The maximum real part of the eigenvalues is presented in Fig. 12(b). It increases with the SCR and crosses zero slightly above SCR=4. The selected cases include a very weak grid case (SCR = 2) and two weak grid cases (SCR = 3 and 4), which remain in the stable region, whereas the stronger grid case (SCR = 10) is unstable. Therefore, these results indicate that the stability of GCIs depends strongly on the interaction between the grid impedance and the characteristics of the control structure used. In contrast, when employing the GFL technique, the converter becomes unstable under weak grid conditions, as reported in [3].

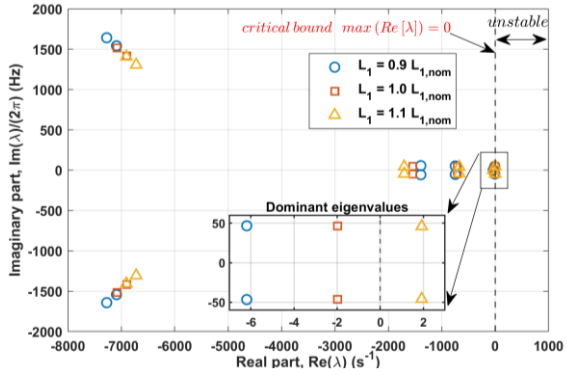
The sensitivity to variations in the LCL filter parameters is examined by varying L_1 and C_f by $\pm 10\%$ from their nominal values. As shown in Fig. 12(c), increasing L_1 moves the dominant eigenvalue pair toward the right-half plane, while decreasing L_1 shifts it further into the left-half plane. The case $L_1 = 1.1L_{1,nom}$ crosses the stability boundary, indicating that L_1 has a considerable influence on the stability margin. In addition, increasing L_1 reduces the frequency of the high-frequency poles.

Fig. 12(d) shows that the displacement of the dominant eigenvalues is smaller under variation of C_f, and all three cases remain in the left-half plane. Increasing C_f results in a smaller reduction in the frequency of high-frequency poles. These results indicate that the system is more sensitive to variations in L_1 than in C_f.

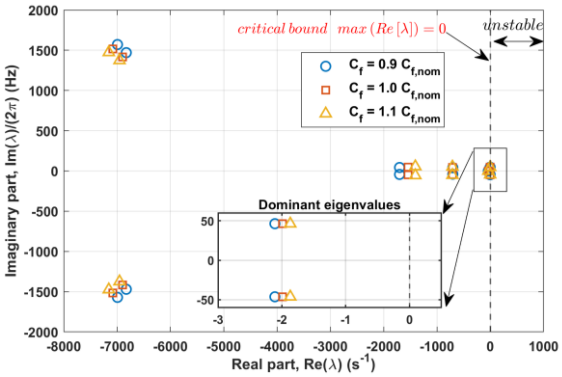


(a) Eigenvalue loci under wide grid-impedance variation (b) Maximum real part of the eigenvalues versus SCR

Fig. 12 Eigenvalue stability analysis and parameter sensitivity of the GFMI



(c) Effect of variation L_1 on a stability



(d) Effect of variation C_f on a stability

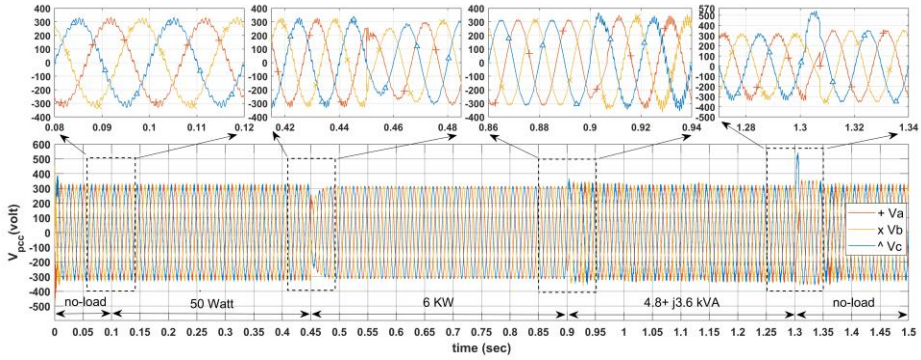
Fig. 12 Eigenvalue stability analysis and parameter sensitivity of the GFMI (continued)

4.4 Simulation results of the GFMI

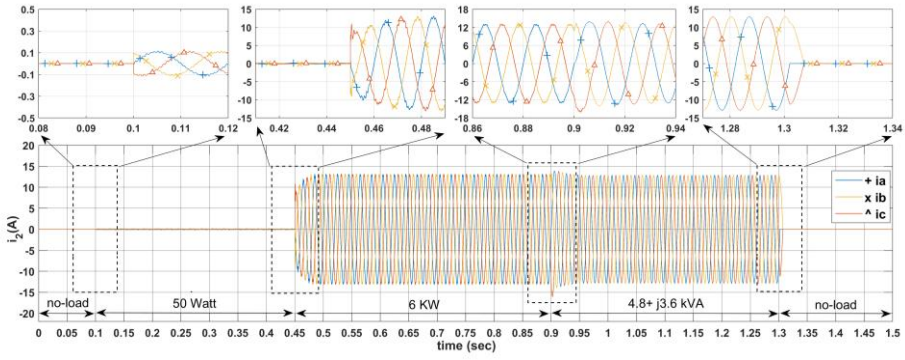
To validate the proposed design methodology, simulation studies were conducted in MATLAB/Simulink R2022b using a detailed switching model of a three-phase two-level voltage-source inverter. The current and voltage controllers were implemented in continuous time. The utility grid was modeled as a balanced three-phase Thevenin equivalent, while the dc-link voltage was assumed to remain constant. The model parameters, switching frequency, and solver configuration are provided in Table 2. The operating scenarios and corresponding results are presented as follows.

(1) Stand-alone mode

The first scenario evaluates GFMI performance in SAM under different loading conditions, as shown in Fig. 13(a). During $t = 0 - 0.1\ s$, the GFMI operates under no-load. During $t = 0.1 - 0.45\ s$, it operates under light-load (50 *W*). Subsequently, during $t = 0.45 - 0.9\ s$ and $t = 0.9 - 1.3\ s$, it operates under nominal load with a resistive load of 6 *kW* and an inductive load of 4.8 *kW*+ *j*3.6 *kVAR*, respectively. Then, it returns to the no-load condition.



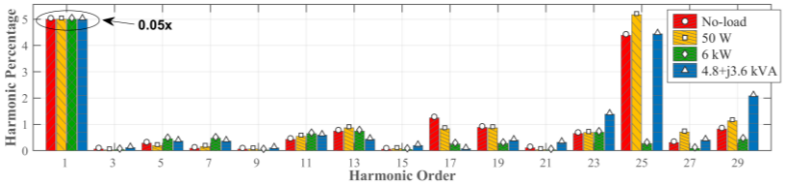
(a) Output voltage waveforms



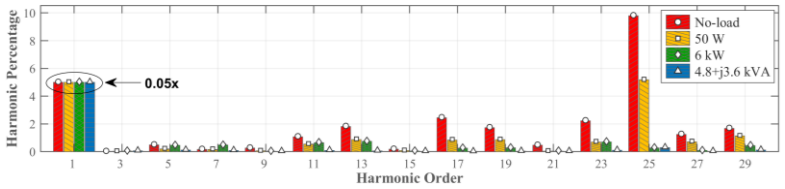
(b) Output current waveforms

Fig. 13 Output waveforms of the GFMI in SAM

As shown in Figs. 13(a) and 13(b), the output voltage and current waveforms ($u_{pcc,abc}$ and $i_{2,abc}$) remain sinusoidal in the steady state. Fig. 13(a) shows a small transient voltage during abrupt load changes. This response indicates the robustness of the voltage controller. It is also observed that the inductive load introduces more waveform distortion than the resistive load. This behavior is related to a shift in the resonance frequency toward lower values, as predicted by Eq. (11), which leads to the amplification of low-order harmonics, as shown in Fig. 14(a).



(a) Output voltage harmonic spectrum

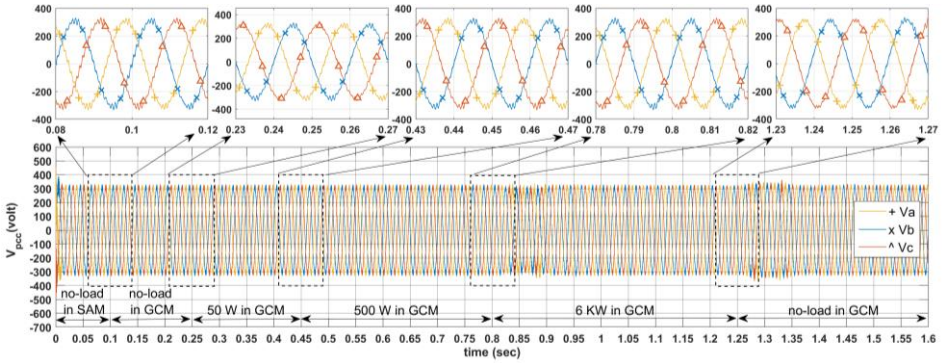


(b) Output current harmonic spectrum

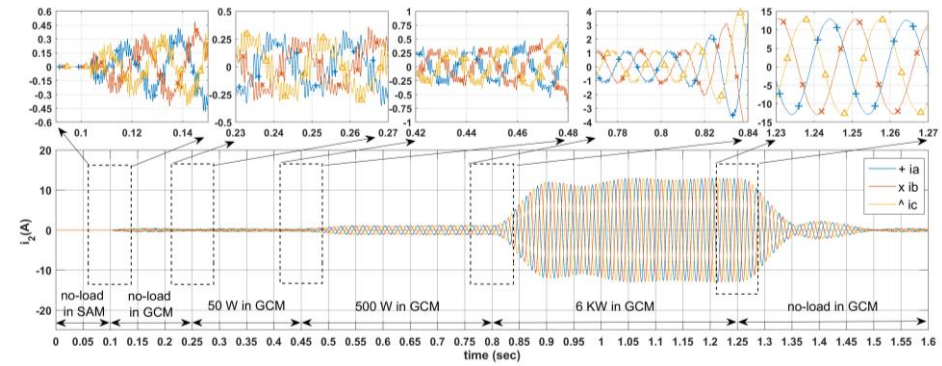
Fig. 14 Harmonic spectrum in SAM

(2) Grid-connected mode

In the second scenario, the GFMI is connected to the grid under the same conditions considered in Section 4.3 (SCR = 4 and $X_g/R_g = 6.3$). The inverter performance is examined under different load conditions in GCM, as illustrated in Fig. 15(a). During $t = 0 - 0.1\ s$, the GFMI operates under no-load. During $t = 0.1 - 0.25\ s$, it is connected to the grid without any power injection command. During $t = 0.25 - 0.45\ s$, the GFMI operates under light-load by injecting real power of 50 W into the grid. Subsequently, during $t = 0.45 - 0.8\ s$ and $t = 0.8 - 1.25\ s$, the injected real power is increased to 500 W and 6 kW, respectively. After $t = 1.25\ s$, the inverter injects zero real power, i.e., it returns to operation in GCM without load.



(a) Output voltage waveforms

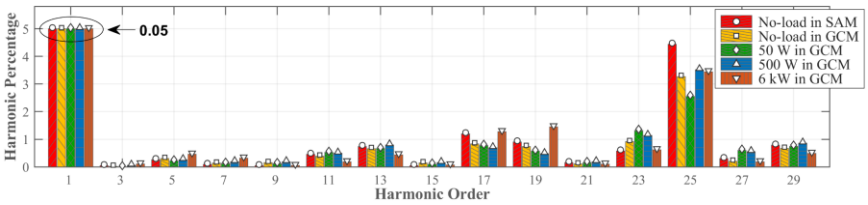


(b) Output current waveforms

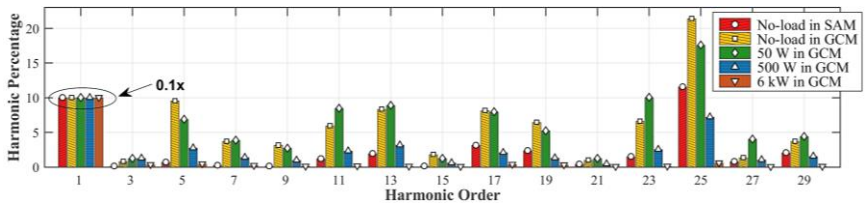
Fig. 15 Output waveforms of the GFMI in GCM

Fig. 15(a) shows that the output voltage waveform remains sinusoidal under all operating conditions. Moreover, Fig. 15(b) demonstrates that the current waveform exhibits a smooth transient response during transitions between these conditions, indicating good tracking performance of the current controller. It can also be observed from Fig. 15(b) that during $t = 0.1 - 0.25\ s$, a small current flows even though the GFMI is commanded to inject zero real power into the grid. This current represents the reactive current absorbed by the LCL filter from the grid. In addition, the current waveform under no-load and light-load conditions shows relatively high distortion due to the absence of load damping. However, this distortion gradually decreases as the injected power increases. Nevertheless, the current waveform remains stable throughout all operating conditions, indicating the effectiveness of the proposed controller and LCL filter design.

The harmonic spectrum of the voltage and current waveforms under these operating conditions in SAM and GCM is shown in Figs. 14 and 16, respectively. The dominant harmonic components in both the voltage and current waveforms appear around the resonance frequency.



(a) Output voltage harmonic spectrum



(b) Output current harmonic spectrum

Fig. 16 Harmonic spectrum in GCM

Table 3 summarizes the total harmonic distortion of the voltage (THD_v) and current (THD_i), and also the total demand distortion for current (TDD_i) under the tested operating conditions. The results show that THD_v complies with the harmonic limits specified in IEEE Std. 519-2022 for all cases [29] . In SAM, THD_i also remains within the standard limit for all tested conditions. In GCM, THD_i satisfies the limit when the GFMI injects 6 kW into the grid. However, it exceeds the limit under no-load and light-load conditions. This increase does not represent a critical issue because the current amplitude is zero or relatively small compared with the nominal-load current, which is consistent with [30]. Therefore, the current harmonic content is further assessed using the total demand distortion (TDD_i), as summarized in Table 3.

Table 3 THD and TDD of the GFMI output voltage and current waveforms under different operating conditions

SAM				GCM			
Operating conditions	THD_v%	THD_i%	TDD_i%	Operating conditions	THD_v%	THD_i%	TDD_i%
no-load	4.99	N/A	N/A	no-load	3.99	30.19	0.7298
50 W	5.79	5.81	0.0482	50 W	3.55	28.21	0.7170
6 KW	1.7	1.7	1.6023	500 W	4.25	9.95	0.7926
4.8+j3.6 KVA	5.68	0.44	0.4346	6 KW	4.3	1.2	1.1138

In a more precise analysis, under these conditions, the TDD_i metric is used instead of the THD_i metric, which represents the percentage of the root-mean-square of the harmonic current content relative to the inverter-rated current (9.11A), as expressed by:

$$TDD_i = \frac{\sqrt{I_2^2 + I_3^2 + I_4^2 + I_5^2 + \ldots}}{I_{rated}} \tag{58}$$

The computed TDD_i values under all conditions are below 5%, demonstrating strict compliance with IEEE Std. 519-2022 for a grid SCR of 4. This indicates that the harmonic current distortion remains within the acceptable level under all tested operating conditions. Therefore, the effect of these harmonic components remains limited. In contrast, the lowest THD_v is obtained under these operating conditions.

To validate the eigenvalue-based stability assessment through time-domain simulations, the designed GFMI is examined under two grid-strength conditions at the same X_g/R_g ratio of 6.3, as shown in Fig. 17. During $t = 0 - 0.8\,s$, the GFMI operates under a weak-grid condition (SCR = 4). Following the initial transient, the voltage and current settle to balanced sinusoidal steady-state waveforms, confirming stable operation. When the SCR is changed to 10 at $t = 0.8\,s$ sustained amplitude oscillations appear in both voltage and current waveforms, indicating instability.

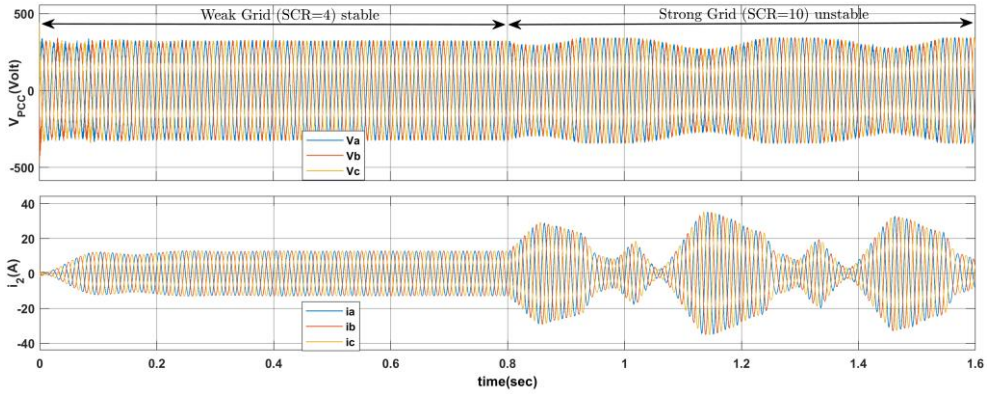


Fig. 17 Time-domain validation of the eigenvalue-based stability assessment during a change in grid strength from SCR = 4 to SCR = 10 at $t = 0.8\,s$: upper, PCC voltages; lower, grid-side currents

These time-domain results are consistent with the stable and unstable operating points predicted by the eigenvalue analysis, as shown in Fig. 12(b). The current waveforms exhibit an oscillatory pattern, which indicates that the power exchange between the GFMI and the grid occurs without regulation. This observed instability results from the reduction in grid impedance, which increases the sensitivity of power exchange. This behavior is inherently associated with two parallel voltage sources having strong characteristics, namely the GFMI and a strong utility grid. To address this issue, a virtual impedance is employed.

5. Conclusions

This paper presented a systematic design procedure and performance evaluation for LCL-filtered GFMIs. The proposed approach included mathematical modeling of the GFMI in the synchronous dq reference frame, LCL filter design based on resonance-frequency constraints, and cascaded controller design using a bandwidth-coordination scheme. Finally, the proposed design was evaluated through eigenvalue-based small-signal stability analysis, and verification in the time domain was conducted under different operating conditions. The main conclusions of this study can be summarized as follows:

(1) The proposed LCL filter design flowchart provides a clear procedure for selecting the filter parameters while verifying the lower and upper resonance-frequency constraints.

(2) The cascaded controller design based on bandwidth coordination reduced the interaction between the inner and outer loops. The analysis indicates that the final bandwidth ratio should be selected based on frequency-domain stability verification and time-domain dynamic performance, rather than by imposing a fixed separation ratio. For the designed GFMI system, the bandwidth ratio is approximately 2.5, providing an acceptable phase margin, good tracking performance, zero steady-state error, and reduced overshoot.

(3) The results from eigenvalue-based stability analysis demonstrate that practical implementation should account for component tolerances and the expected grid-strength range during component selection and controller tuning.

(4) The simulation results demonstrate that the output voltage maintains low harmonic distortion under all tested conditions. Additionally, the corresponding TDD of the output current remains below 5%, including no-load and light-load conditions.

(5) The proposed design methodology provides a practical framework for designing GFMIs intended to operate in grids subject to frequent and stochastic outages. It may also serve as a useful design reference for researchers and engineers.

Future work should investigate the influence of abnormal operating conditions on the small-signal stability of the output voltage and frequency. Another important aspect for future investigation is the compatibility of the proposed design procedure with fault-ride-through capability, which is one of the key design requirements for GFMIs. Additionally, the proposed GFMI design should be experimentally validated using a laboratory prototype to verify its practical applicability under real operating conditions.

Acknowledgments

The authors would like to thank the University of Mosul, College of Engineering, for their support, which enabled us to complete this research successfully.

Conflicts of Interest

The authors declare no conflict of interest.

References

[1] V. V. Babu, J. P. Roselyn, C. Nithya, and P. Sundaravadivel, “Development of Grid-Forming and Grid-Following Inverter Control in Microgrid Network Ensuring Grid Stability and Frequency Response,” Electronics, vol. 13, no. 10, article no. 1958, 2024.

[2] Y. Zhang, C. Song, T. Wang, and K. Wang, “Optimization of Passive Damping for LCL-Filtered AC Grid-Connected PV-Storage Integrated Systems,” Electronics, vol. 14, no. 4, article no. 801, 2025.

[3] X. Gao, D. Zhou, A. Anvari-Moghaddam, and F. Blaabjerg, “Seamless Switching Method between Grid-Following and Grid-Forming Control for Renewable Energy Conversion Systems,” IEEE Transactions on Industry Applications, vol. 61, no. 1, pp. 597-606, 2025.

[4] I. Bennia, E. Elbouchikhi, A. Harrag, Y. Daili, A. Saim, A. E. M. Bouzid, et al., “Design, Modeling, and Validation of Grid-Forming Inverters for Frequency Synchronization and Restoration,” Energies, vol. 17, no. 1, article no. 59, 2024.

[5] X. Jia, S. Yu, Y. Zhang, Y. Feng, and B. Zhou, “LCL Grid-Connected Inverter Resonance Feedforward-Active Damping Hybrid Control Strategy for Mitigating Weak Grid Resonance and Harmonic Currents,” Energies, vol. 18, no. 22, article no. 6010, 2025.

[6] H. Alrajhi, S. A. Raza, H. Babsail, and A. Alattas, “Design, Analysis and Comprehensive Assessment of LCL Filters for VSC Applications,” Journal of Umm Al-Qura University for Engineering and Architecture, vol. 16, no. 3, pp. 559-573, 2025.

[7] M. Saleem, K. Y. Choi, and R. Y. Kim, “Resonance Damping for an LCL Filter Type Grid-Connected Inverter with Active Disturbance Rejection Control under Grid Impedance Uncertainty,” International Journal of Electrical Power & Energy Systems, vol. 109, pp. 444-454, 2019.

[8] N. Rasekh and M. Hosseinpour, “LCL Filter Design and Robust Converter Side Current Feedback Control for Grid-Connected Proton Exchange Membrane Fuel Cell System,” International Journal of Hydrogen Energy, vol. 45, no. 23, pp. 13055-13067, 2020.

[9] D. Chen, S. Zhang, and H. Lin, “An Active Damping Control Strategy for Suppressing LCL Resonant Point Migration for Three-Phase Grid-Tied Inverter,” Scientific Reports, vol. 14, no. 1, article no. 22911, 2024.

[10] M. Cengiz and T. Duman, “Sliding Mode Control for a Single-Phase Grid-Connected H-Bridge NPC Inverter with a Symmetrical LCL Filter,” Computers and Electrical Engineering, vol. 117, article no. 109298, 2024.

[11] M. Ijaz, R. Nazir, M. Alhussein, J. Ahmad, K. Aurangzeb, and F. Saleem, “Digital Resonant Control of Power Converters under Variable Grid Frequency Conditions,” Frontiers in Energy Research, vol. 11, article no. 1272329, 2023.

[12] M. Parvez, M. F. M. Elias, N. A. Rahim, F. Blaabjerg, D. Abbott, and S. F. Al-Sarawi, "Comparative Study of Discrete PI and PR Controls for Single-Phase UPS Inverter," IEEE Access, vol. 8, pp. 45584-45595, 2020.
[13] M. H. Ravanji, D. B. Rathnayake, M. Z. Mansour, and B. Bahrani, "Impact of Voltage-Loop Feedforward Terms on the Stability of Grid-Forming Inverters and Remedial Actions," IEEE Transactions on Energy Conversion, vol. 38, no. 3, pp. 1554-1565, 2023.
[14] O. Babayomi, Y. Li, Z. Zhang, and K. B. Park, "Advanced Control of Grid-Connected Microgrids: Challenges, Advances, and Trends," IEEE Transactions on Power Electronics, vol. 40, no. 6, pp. 7681-7708, 2025.
[15] M. Liserre, F. Blaabjerg, and S. Hansen, "Design and Control of an LCL-Filter-Based Three-Phase Active Rectifier," IEEE Transactions on Industry Applications, vol. 41, no. 5, pp. 1281-1291, 2005.
[16] A. Reznik, M. G. Simões, A. Al-Durra, and S. M. Muyeen, "LCL Filter Design and Performance Analysis for Grid-Interconnected Systems," IEEE Transactions on Industry Applications, vol. 50, no. 2, pp. 1225-1232, 2014.
[17] H. H. Abbas, Q. Shafiee, and H. Bevrani, "Optimal Passive LCL Filter Design for Grid-Connected Converters in Weak Grids," Electric Power Systems Research, vol. 235, article no. 110896, 2024.
[18] M. H. Rashid, Power Electronics Handbook, 4th ed., Oxford: Butterworth-Heinemann, 2017.
[19] M. H. Mahlooji, H. R. Mohammadi, and M. Rahimi, "A Review on Modeling and Control of Grid-Connected Photovoltaic Inverters with LCL Filter," Renewable and Sustainable Energy Reviews, vol. 81, part 1, pp. 563-578, 2018.
[20] Y. Han, M. Yang, H. Li, P. Yang, L. Xu, E. A. A. Coelho, et al., "Modeling and Stability Analysis of LCL-Type Grid-Connected Inverters: A Comprehensive Overview," IEEE Access, vol. 7, pp. 114975-115001, 2019.
[21] S. Albatran, A. Koran, I. A. Smadi, and H. J. Ahmad, "Optimal Design of Passive RC-Damped LCL Filter for Grid-Connected Voltage Source Inverters," Electrical Engineering, vol. 100, no. 4, pp. 2499-2508, 2018.
[22] J. Jo and H. Cha, "Design of Effective Passive Damping Resistor of Grid-Connected Inverter with LCL Filter for Industrial Applications," Journal of Electrical Engineering & Technology, vol. 14, no. 5, pp. 2039-2048, 2019.
[23] A. Yazdani and R. Iravani, Voltage-Sourced Converters in Power Systems: Modeling, Control, and Applications, 1st ed., Hoboken, NJ: IEEE Press/John Wiley & Sons, 2010.
[24] H. Alrajhi, Y. Al-Harbi, A. Al-Zahrani, S. A. Raza, A. Daraz, and M. Al-Kaabi, "Comprehensive Analysis of PI Tuning Techniques for VSC Applications," Journal of Umm Al-Qura University for Engineering and Architecture, vol. 16, no. 3, pp. 599-616, 2025.
[25] C. Bajracharya, "Control of VSC-HVDC for Wind Power," Master's thesis, Department of Electrical Power Engineering, Norwegian University of Science and Technology, Trondheim, Norway, 2008.
[26] R. Ali, H. Heydari-doostabad, S. Sajedi, and T. O'Donnell, "Improved Design of Passive Damping for Single Phase Grid-Connected LCL Filtered Inverter Considering Impedance Stability," IET Power Electronics, vol. 17, no. 4, pp. 511-523, 2024.
[27] C. Yanarates and Z. Zhou, "Symmetrical Pole Placement Method-Based Unity Proportional Gain Resonant and Gain Scheduled Proportional (PR-P) Controller with Harmonic Compensator for Single Phase Grid-Connected PV Inverters," IEEE Access, vol. 9, pp. 93165-93181, 2021.
[28] L. M. Engan, S. Ekrheim, S. Bjarghov, J. R. A. Klemets, I. Schytte, and G. Kjølle, "Reference Dataset for Semi-Urban and Rural Norwegian Low Voltage Distribution Grids," Data in Brief, vol. 59, article no. 111453, 2025.
[29] IEEE Standard for Harmonic Control in Electric Power Systems, IEEE Standard 519, 2022.
[30] Y. Du, D. D. C. Lu, G. James, and D. J. Cornforth, "Modeling and Analysis of Current Harmonic Distortion from Grid Connected PV Inverters under Different Operating Conditions," Solar Energy, vol. 94, pp. 182-194, 2013.



Copyright© by the authors. Licensee TAETI, Taiwan. This article is an open access article distributed under the terms and conditions of the Creative Commons Attribution (CC BY-NC) license (https://creativecommons.org/licenses/by-nc/4.0/).